


Mechanical performance and supermolecular morphology of void free polypropylene manufactured by fused filament fabrication

Miaozi Huang¹ | Yao Xu¹ | Alois K. Schlarb^{1,2,3} 

¹Chair of Composite Engineering (CCe), Technische Universität Kaiserslautern (TUK), Kaiserslautern, Germany

²Research Center OPTIMAS, Technische Universität Kaiserslautern (TUK), Kaiserslautern, Germany

³Qingdao University of Science & Technology, Qingdao, China

Correspondence

Alois K. Schlarb, Chair of Composite Engineering (CCe), Technische Universität Kaiserslautern (TUK), Gottlieb-Daimler-Str. Bld. 44, 67663 Kaiserslautern, Germany.
Email: alois.schlarb@mv.uni-kl.de.

Abstract

It is known from the literature that freedom from macroscopic defects (voids) is an essential prerequisite for good mechanical properties of 3D-printed components manufactured using fused filament fabrication. The present study further shows that the morphology and mechanical properties of void free components are significantly influenced by the choice of process parameters. Components that were printed at low temperatures and high speeds show fair and inhomogeneous supermolecular morphology, clearly visible weld seams and a special flow-induced staggered structure of the individual strands laid-up. At higher magnification in the optical microscope, transcrystalline structures are visible starting from the contact area between the strands, that is, crystallization has started at the interface between the strands and is moving forward towards the center of the strands. In contrast, the samples printed at high temperatures and low speeds show a homogeneous supermolecular morphology with overall larger spherulites and a higher degree of crystallinity and compared to the specimens printed with the low temperature/high speed-set much better mechanical properties. A numerical simulation of the temperature at the contact point of the strand emerging from the hot nozzle and the cooled strand neighbor agrees well with the measured behavior. The thermal simulation thus enables the temperature to be calculated at any point in time in the welding contact and thus access to the local thermal conditions during joining, cooling and the formation of the morphology.

KEYWORDS

3D-printing, polyolefins (polypropylene), simulation, supramolecular morphology, structure-property-relations

1 | INTRODUCTION

Fused filament fabrication (FFF), one of the most promising additive manufacturing or 3D printing technology,

has gained great attention in manufacturing plastic components in recent years, since it provides several advantages such as shortening of the production development cycle, demand-driven production of components, moldless

This is an open access article under the terms of the Creative Commons Attribution License, which permits use, distribution and reproduction in any medium, provided the original work is properly cited.

© 2021 The Authors. *Journal of Applied Polymer Science* published by Wiley Periodicals LLC.

manufacturing, low material waste rate, and so on. A variety of commercially available polymeric materials, such as polylactic acid (PLA),^{1,2} acrylonitrile butadiene styrene (ABS),^{3,4} polycarbonate (PC),^{5,6} polyethylene terephthalate glycol-modified (PETG),⁷ polyamide (PA),⁸ even polyetheretherketone (PEEK)^{9,10} have been applied to print components for academic research and industry applications. Besides, polypropylene (PP) has attracted increasing attention on its manufacture by using FFF process,^{11–14} due to its low cost, low density, excellent chemical resistance, and so on.

During FFF process, a thermoplastic filament is melted in a heated nozzle, which deposits polymer strands according to pre-defined path layer-by-layer. Similar to the traditional extrusion welding technique, melted strands are placed against those previously deposited and already cooled strands to weld them together. Hence, a typical FFF manufactured component consists of deposited strands, enclosed voids and weld lines, which lead to varying structure and ultimately determine mechanical properties.^{13,15} It is commonly accepted that the resulted weld quality is generally dominated by the local flow and complex thermal distribution during deposition process, which in turn depends on the process conditions.^{16–19} Therefore, in recent years efforts have been made to improve the weld formation by controlling process condition during FFF process such as, using a square nozzle, raising nozzle and platform temperature, slow-down printing speed and reduction of layer thickness, which are generally revealed by analysis of the mesostructure features.^{18,20–28} These typical mesostructure features provide the information, that is, the void content/size^{29,30} and the length of welding lined between layers^{31–33} during FFF process. It was revealed that the tensile strength, Young's modulus can be improved up to 60% and 160% by reducing void content, respectively.^{20,29,34,35} It has to be pointed out that the general mesostructured features enable us only basic knowledge. In the present work, we prepared PP specimens by FFF technique under four representative process conditions aiming to extensively explore the relation between process conditions, supermolecular morphology and

mechanical properties with respect to the local flow and temperature distribution during the process. Furthermore, thermal simulation was also carried out to deeply understand the effect of local temperature history on the morphology of 3D printed structures.

2 | MATERIALS AND METHODS

Pellets of commercial polypropylene (HD 120MO, Borealis GmbH, Burghausen, Germany) were used in this study. Using DSC, we determined a melting temperature of $T_m = 162^\circ\text{C}$. The crystallization temperature T_c was 116°C . According to,³⁶ the average molecular mass M_w of the used polypropylene is 365 kg/mol and its polydispersity $M_w/M_n = 5.4$. From the pellets, a well-defined filament with diameter $d = 1.7 \pm 0.05$ mm were fabricated via a single screw extruder (EX6, Filabot, Barre). The temperatures at the barrel were selected as 40/130/200/195°C from the hopper to the nozzle. The screw speed was set 6 rpm. The specimens were printed via a modified FFF 3D printer (Ultimaker 2, Ultimaker B.V., Utrecht, Netherlands) with 0.4 mm nozzle diameter. The bar-shaped bodies with a dimension of $50 \times 4 \times 2$ mm³ are printed perpendicularly to the longitudinal direction. An overview of the whole processing chain is shown in Figure 1.

In order to investigate the morphology of void-free 3D printed components two completely different sets of nozzle temperature, platform temperature and printing speed was selected based on preliminary tests. In the preliminary tests, a large number of parameter variations were carried out and the properties of the manufactured specimens were comparatively evaluated by means of tensile tests and thermoanalytical measurements using analysis of variance (ANOVA). The criterion for the selection of the parameters for the deeper investigation of morphology and properties as well as for the simulation of the temperature profiles in this paper were the parameter sets that had led to the best and worst mechanical properties and the integrally highest and lowest degrees of crystallinity. With the

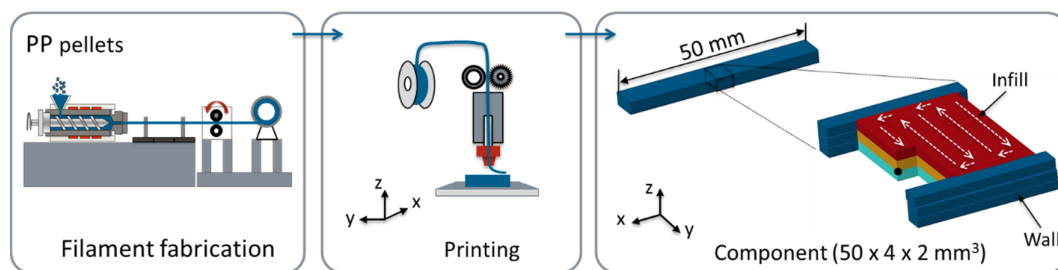
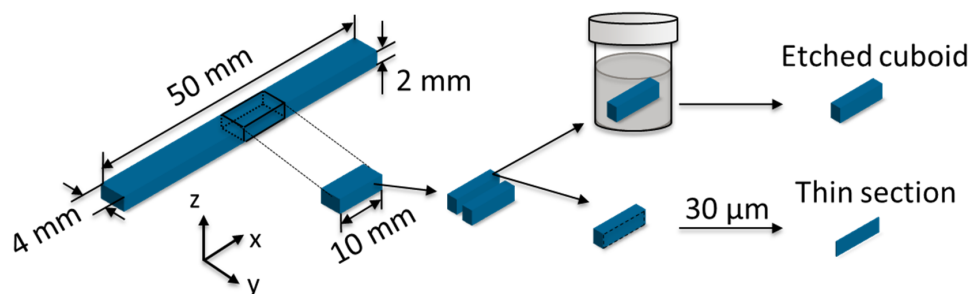


FIGURE 1 Schematic illustration of the whole processing chain. The fixed black point (right) at $(x = 0$ mm, $y = 0$ mm, $z = 0.2$ mm) was chosen for display the temperature profiles during the printing processes [Color figure can be viewed at wileyonlinelibrary.com]

TABLE 1 3D printing parameters

Process condition	Nozzle temperature °C	Platform temperature °C	Printing speed mm/s	Layer thickness mm	Infill %
Low	200	60	60	0.1	100
	200	60	60	0.2	100
High	245	100	10	0.1	100
	245	100	10	0.2	100

FIGURE 2 Preparation of the specimens [Color figure can be viewed at wileyonlinelibrary.com]



"Low" setting, the combination of nozzle temperature, platform temperature and printing speed was chosen so that specimens could just be printed without visible voids. The combination "High", that is, high nozzle temperature, high platform temperature and low printing speed, guarantees both freedom from voids and the highest possible temperature during strand deposition, that is, during contact between the extruded strand and the previously deposited strand. These two different sets were applied with two different layer thicknesses and with an infill of 100%, as listed in Table 1.

To overcome the warpage during printing, the first layer of the samples was printed with a brim on a PP tape (tesa 64,014).

Tensile tests of the samples were conducted in the longitudinal direction (in x-direction) on a universal tensile testing machine based on the international standard DIN ISO EN 527. The crosshead speed was set at 1 mm/min in the range $\epsilon = 0 \dots 0.25\%$ using an extensometer for determining the tensile modulus and set at 50 mm/min for determining the tensile strength. All the data presented correspond to the mean value of at least five measurements.

To investigate the supermolecular morphology, the prepared samples were cut by a rotation microtome (Hyrax M 25, Carl Zeiss, MicroImaging GmbH, Jena, Germany) and then chemically etched in a chemical solution, which contained potassium permanganate, sulfuric acid and phosphoric acid^{37,38} as shown in Figure 2.

Afterwards, the chemical-etched surfaces were inspected by using an optical microscope (OM) (Nikon ECLIPSE LV100POL, Nikon GmbH, Düsseldorf, Germany) and a Keyence confocal 3D laser scanning

microscope (LSM, VK-X1050, Keyence Corporation, Japan) operated in reflected mode. For measuring the average diameter of the spherulite, at least three samples were measured according to the ASTM E11210 standard for grain size determination. In parallel, the development of the supermolecular morphology was observed using an OM in transmission mode equipped with a hot stage (LTS 420, Linkam, Surrey, England). The 30 μm thin films cut by the microtome were heated from room temperature to 178°C at 20 K/min and hold for 10 mins. Afterwards, for non-isothermal crystallization the specimens were cooled to room temperature 23°C at 10 K/min.

The thermal properties of the polymers and composites were analyzed by a differential scanning calorimetry (DSC Q20, TA Instruments). The thermal investigations were carried out under nitrogen atmosphere with a flow rate of 50 ml/min and performed from 40 to 220°C with a heating/cooling rate of 10 K/min. The degree of crystallinity X_m for the PP phase was determined by using the following equation:

$$X_m = \frac{\Delta H_m}{\Delta H_m^0} \cdot 100\% \quad (1)$$

where ΔH_m is the measured melting enthalpy, and ΔH_m^0 is the theoretical specific enthalpy of completely crystallized PP (207 J/g).

In order to estimate the temperature development during the FFF process and, more importantly, to reduce the experimental efforts, thermal simulations of the time-dependent temperature evolution of the printed part were performed by using a commercially available

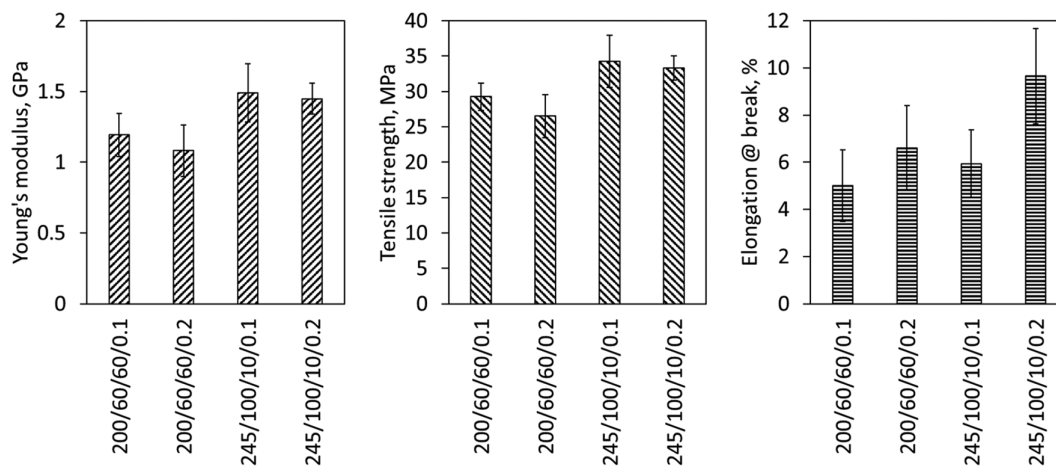


FIGURE 3 Tensile properties of samples printed under different process conditions (nozzle temperature/platform temperature/printing speed/layer height)

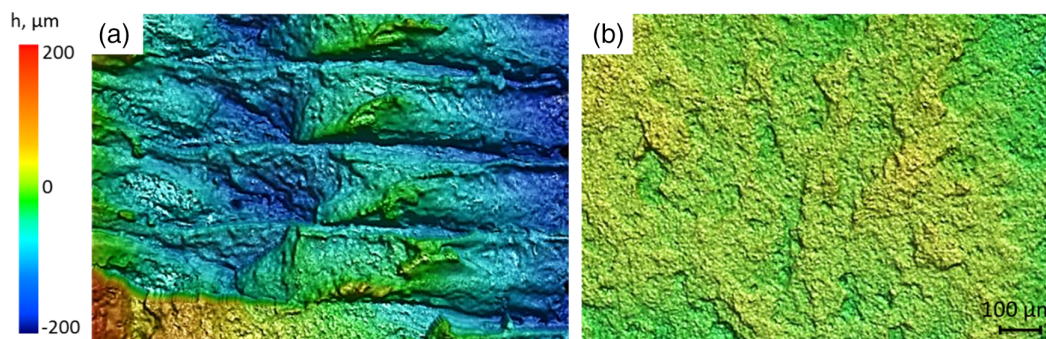


FIGURE 4 3D laser scanning microscope images with height information of tensile fracture surfaces (in yz-plane) of the samples printed under process conditions (a) 200/60/60/0.2 and (b) 245/100/10/0.2 (nozzle temperature/platform temperature/printing speed/layer height) [Color figure can be viewed at wileyonlinelibrary.com]

CAE-Software ANSYS® 2019R1. Geometric model was created concerning for the real printing part, however, in order to reduce the highly time-consuming simulation process, only half of the sample (cf. Figure 1) was modeled, which is $50 \times 4 \times 1 \text{ mm}^3$. For calculating the temperature evolution of the printed sample, the heat transfer during the printing process can be described by using the following differential equation:

$$\frac{\partial}{\partial x} \left(\lambda_{xx} \frac{\partial T}{\partial x} \right) + \frac{\partial}{\partial y} \left(\lambda_{yy} \frac{\partial T}{\partial y} \right) + \frac{\partial}{\partial z} \left(\lambda_{zz} \frac{\partial T}{\partial z} \right) + \dots q = \rho(T) \cdot C(T) \cdot \frac{dT}{dt} \quad (2)$$

where x , y , and z are the coordinates, λ , ρ , C , and T are thermal conductivity, density, specific heat capacity and temperature, respectively, as well as the time t and the heat generation rate $\dots q$. Based on the temperature analysis, the impact of the temperature evolutions during the printing process can be assessed. For calculating the dynamic temperature evolution of the printed layers,

temperature-dependent thermal properties of PP were incorporated into the model (cf. Figure S1). The heat transfer from the printed body to air is applied as:

$$\dot{q} = \alpha \cdot (T - T_{air}) \quad (3)$$

where \dot{q} is heat transfer, the heat convection coefficient between polymer and air is indicated by α , which was set at $12.1 \text{ W/m}^2 \cdot \text{K}$ calculated by Nusselt-number referred to free convection. T_{air} denotes the air temperature surrounding the specimen, set 5°C lower than the platform temperature based on the measurements. To simplify the models, the calculations are based on the following hypotheses:

- The melt temperatures are equal to the nozzle temperature.
- FFF printed parts are pore-free, strands are fully contacted with each other and therefore no contact heat resistance.
- The influences of heat radiation, polymer crystallization and thermal expansion are neglected.

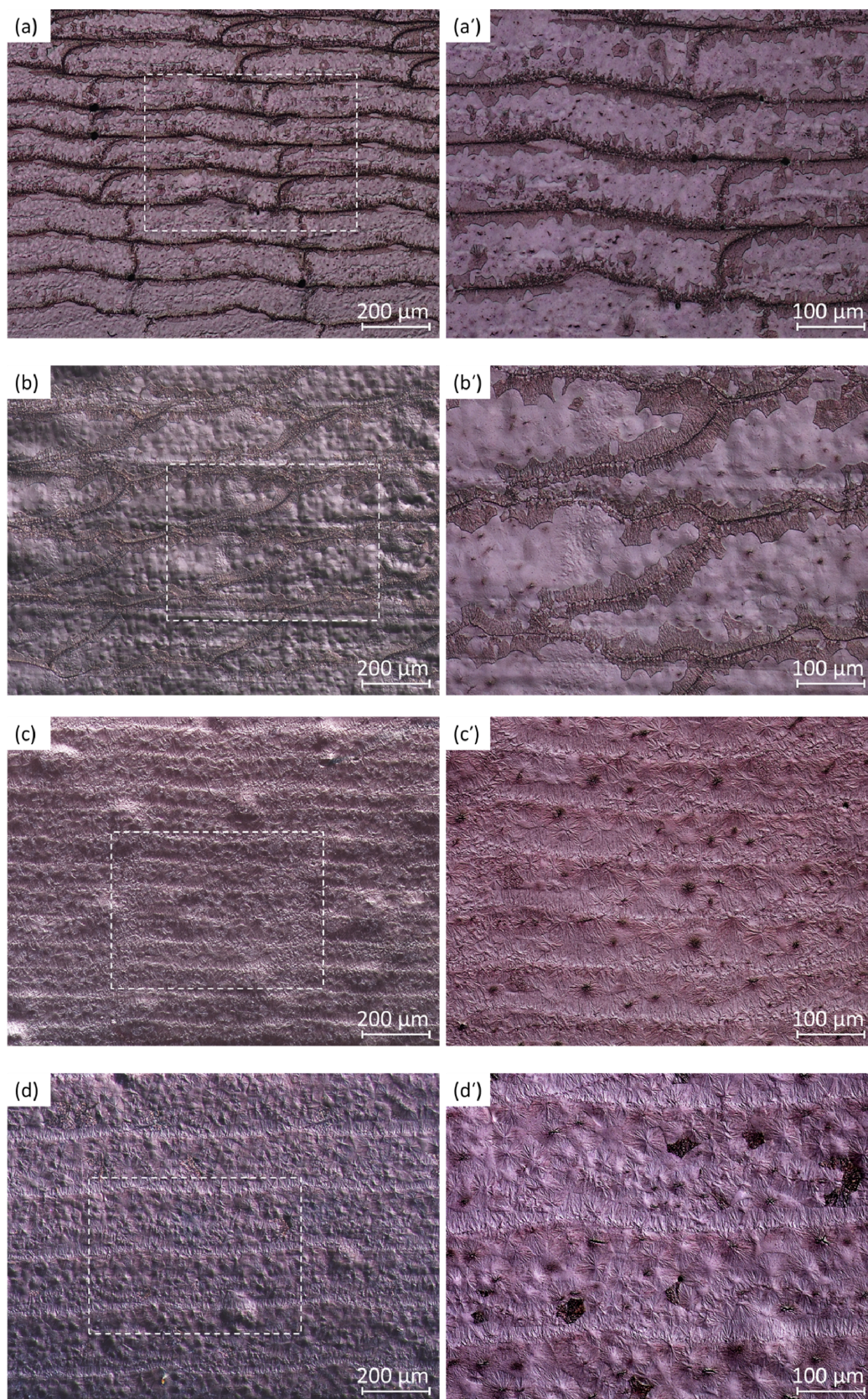


FIGURE 5 Morphology of printed PP specimens in xz -plane (cf. Figure 1) after chemical etching, which were printed with the parameters of (a, a') 200/60/60/0.1, (b, b') 200/60/60/0.2, (c, c') 245/100/10/0.1, and (d, d') 245/100/10/0.2 (nozzle temperature/platform temperature/printing speed/layer height). Strands printing were sequenced from right to left [Color figure can be viewed at wileyonlinelibrary.com]

3 | RESULTS AND DISCUSSION

3.1 | Mechanical properties

Figure 3 shows the mechanical properties of uniaxial, static tensile tests of specimens printed under different conditions (tested in the x-direction). As is seen, process conditions have a substantial effect on the tensile properties. The specimens printed with "High" setting exhibit higher Young's modulus and tensile strength. The samples printed with 245/100/10/0.1 (nozzle temperature/platform temperature/printing speed/layer height) present the highest Young's modulus and tensile strength, which are around 38% and 30% higher than those printed with 200/60/60/0.2, respectively. It is also worth of noting that the specimens with smaller layer height show overall slightly higher mean values of Young's modulus and tensile strength than those with larger layer height at the same printing conditions, which is due to transverse strain restraint of the different supermolecular morphology of the weld zones. In the same material volume, there are less and (at higher temperatures) almost invisible weld zones with a larger printing layer thickness and thus a comparatively higher elongation at break but a lower Young's modulus. Therefore the specimens printed with "High" setting 245/100/10/0.2 are tougher than those printed under other conditions, which can also be inferred by the tensile fracture surfaces (Figure 4). In contrast, the samples printed with "Low" setting still keep the visible weld line, which indicates a weak interfacial welding strength between strands, resulting in poor tensile properties.

3.2 | Morphology

Figure 5 shows the morphology of the etched cross section of the printed components (in xz-plane, cf. Figure 1) under different printing conditions. First of all, it is noticeable that the process conditions exerted significant influence on the morphologies of the printed samples, even if all samples are approx. Void-free. The welding line in the samples printed with "Low" setting (Figure 5(a),(b)) is more pronounced than those printed with "High" setting (Figure 5(c),(d)). Specifically, a remarkable staggered and overlapping structure was observed. This phenomenon is presumably due to the local flow and deformation of the polymer strands during the deposition process. During the process, the melted polymer strands are placed on the pre-defined paths, due to constrained flow partially occupied by previously deposited strands, and therefore squeezed to form into the particular structure, as schematized in Figure 6. A close view of the morphology clearly demonstrates that a highly oriented crystalline structure at the weld region is

formed perpendicular to the weld line (Figure 5(a'),(b)'), which are extremely similar to a transcrystalline structure of PP in the vicinity of fiber induced by shear.^{39,40} Accompanied with the transcrystalline structure usually appear β -modification as well. In contrast, the samples printed with "High" setting exhibit a very homogeneous morphology without a clear weld line (Figure 5(c')(d)'), thus implying a superior weld strength. As a result, the mechanical properties of the parts are improved, as discussed above. It is worthy of noting that, based on the qualitative analysis the samples printed with "High" setting present the bigger spherulite size than the corresponding value of specimens printed with "Low" setting (Figure 7). In addition, samples printed with smaller layer height shows a smaller mean spherulite size. All the above are presumably due to the complex temperature history during the process. Therefore, the analysis of temperature profiles was carried out (see later discussion).

Figure 8 shows the development of the spherulitic structure of the samples under polarized light in a hot

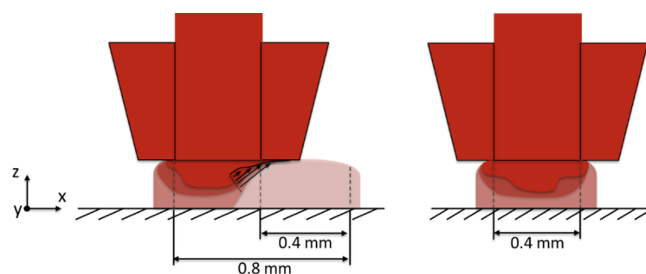


FIGURE 6 Schematic illustration of the local flow and deformation during deposition process [Color figure can be viewed at wileyonlinelibrary.com]

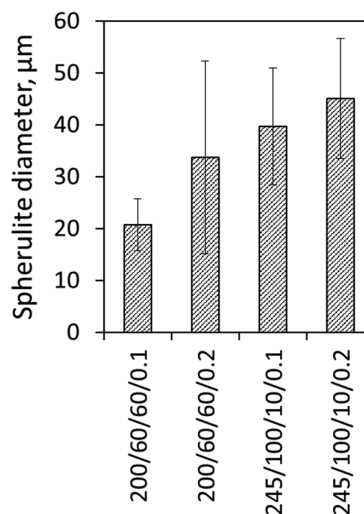


FIGURE 7 Variation of average spherulite size of printed specimens under different process conditions (nozzle temperature/platform temperature/printing speed/layer height)

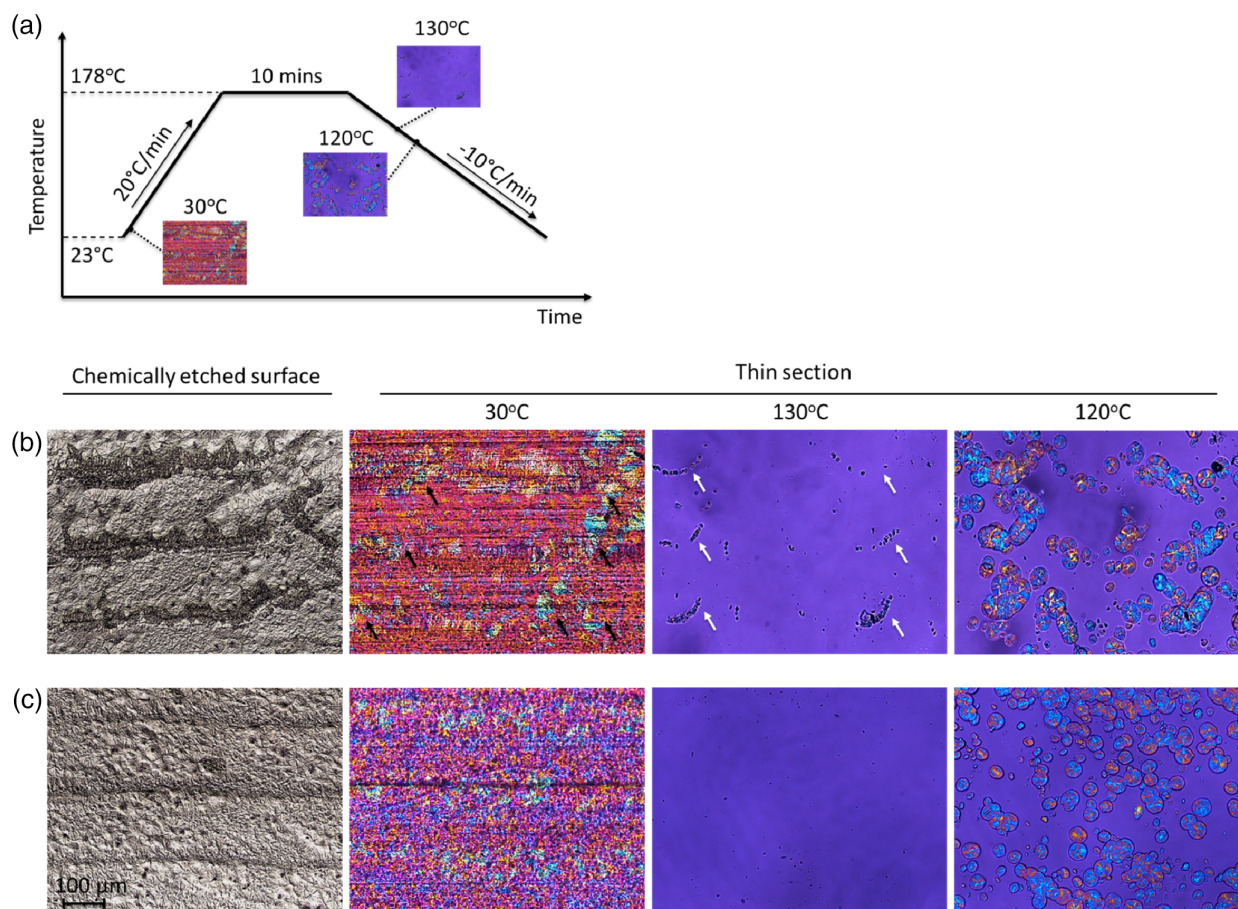


FIGURE 8 (a) Illustration of the non-isothermal crystallization of the prepared thin sections in a hot stage. Optical micrographs of the chemically etched cut surfaces under reflecting light and spherulite development of thin sections in xz-plane under polarized light. Printing conditions: (b) 200/60/60/0.2 and (c) 245/100/10/0.2 (nozzle temperature/platform temperature/printing speed/layer height) [Color figure can be viewed at [wileyonlinelibrary.com](https://onlinelibrary.wiley.com)]

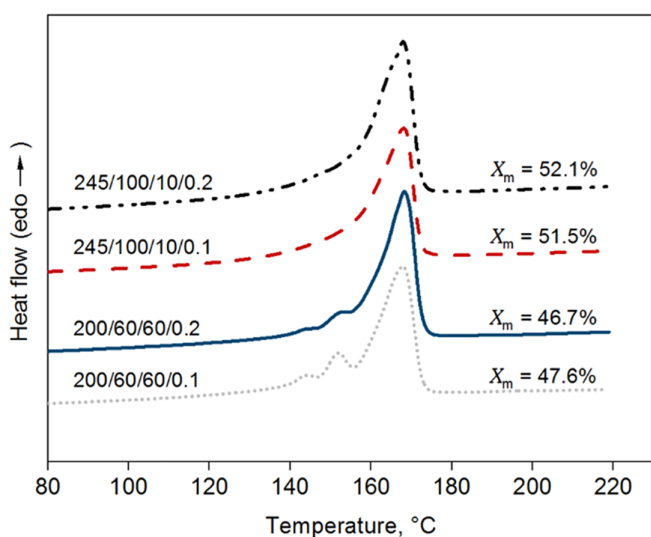


FIGURE 9 DSC 1. Heating curves of PP printed under various process conditions (nozzle temperature/platform temperature/printing speed/layer height) [Color figure can be viewed at [wileyonlinelibrary.com](https://onlinelibrary.wiley.com)]

stage. The pictures are taken at the beginning of the heating (at 30°C) and during the cooling from the melt at temperatures (130 and 120°C) (cf. Figure 8(a)). Similar to the etched samples printed with "Low" setting, the prepared thin films also exhibit an inhomogeneous morphology at 30°C. In the weld regions, some brighter spherulites can be observed, is indicated by the black arrows in Figure 8(b). It is well worth pointing out that the spherulites are first visible at 130°C in the welding area denoted by the white arrow, where the unique overlapping structure formed by the constrained material flow as discussed beforehand (cf. Figure 5(b),(b')). It can be recognized more clearly that at 120°C the most spherulites appear in the welding area. In contrast, the specimens printed with "High" setting are still fully molten at 130°C and the spherulites are distributed more homogeneously at 120°C. The results suggest that the samples in the melt still retain a partial memory of their previous crystalline structure, which is also called melt memory applied by several researchers to study the flow-, drawing- and processing-

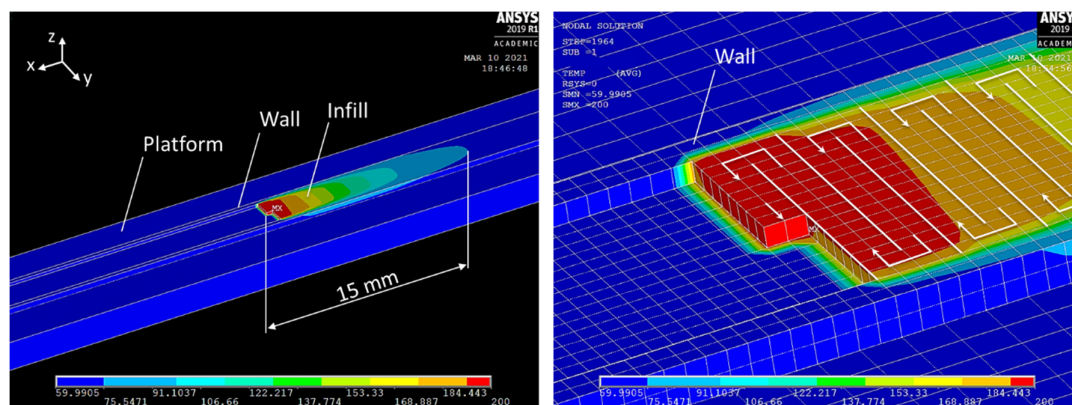


FIGURE 10 Dynamic temperature simulation of the FFF process with 200/60/60/0.2 (nozzle temperature/platform temperature/printing speed/layer height). Element edge length of 3D printed model is 0.2 mm [Color figure can be viewed at [wileyonlinelibrary.com](https://onlinelibrary.wiley.com/doi/10.1002/app.511409)]

induced crystalline structure.^{41–44} Specifically, in the specimens printed with "Low" setting all thermally sensitive nuclei are destroyed, leaving only at the weld region the temperature-resistant stable nuclei, which presumably induced by the flow and temperature gradient during deposition process. Accordingly, the nuclei survived in the melt accelerate the crystallization resulting in the early appearance of the spherulites in the weld area.

Figure 9 depicts the plots of first heating curves of the DSC measurements of the samples printed under the different process conditions. It can be clearly seen that DSC curve of the samples printed with "Low" setting demonstrate double peaks between 140 and 160°C, while no additional peak in the temperature area was found from those printed with "High" setting. The first peak was reported to be the β -modification, which is generally formed at higher undercooling or high shear rates.^{26,45,46} The second peak can be corresponded to β' -modification formed essentially from the heating of DSC test itself where β -modification formed first and recrystallized into a more stable structure β' -modification before transform into the α -modification.¹³ Besides, the percentage of crystallinity (X_m) of the specimens printed with "High" setting is obviously higher than those printed with "Low" setting. The low degree of crystallinity and the existence of β -modification in the samples printed with "Low" setting can correlate to the low Young's modulus and tensile strength.^{26,47,48}

3.3 | Temperature simulations

In order to reveal a possible relationship between the local temperature evolution and the morphology, numerical simulations of the temperature were performed for the "Low" (200/60/60/0.2) and "High" (245/100/10/0.1) process conditions, which have the lowest and best mechanical properties, respectively. In the simulation, as

in the experiment, the circumferential contour (wall) is printed first and then the inner area is filled with a meandering nozzle movement. Figure 10 shows an example of the temperature distribution in the sample at the time when half of the infill of the second layer is printed.

It can be clearly seen that the nozzle trails a temperature field above the ambient temperature. In fact, under the selected conditions, a field above $T = 60^\circ\text{C}$ extends over a length of about 15 mm with a width of 4 mm. Temperatures above the melting temperature of polypropylene can be seen up to 2 mm away from the nozzle.

Figure 11 displays the temperature profiles at the reference point ($x = 0$ mm, $y = 0$ mm, $z = 0.2$ mm) in the center of the sample indicated by the black point. As the nozzle moves further and further away in the x -direction during printing, the temperature at the reference point decreases progressively to platform temperature until the nozzle again reaches the position one layer thickness above the reference point. Then the point sees another temperature peak and again another drop to platform temperature. This cycle repeats layer after layer, with the temperature level dropping at each cycle, that is, with increasing distance from the reference point. Interestingly, double peaks of the temperature can be observed two times in the enlarged view in Figure 11(b), where i.e. L1st and L2nd indicate the temperature profile of first layer through the fixed point and the layer above with "Low" setting, respectively. Similarly are the H1st and H2nd with "High" setting. This observation can be attributed to that the location for plotting the temperature profiles are specially selected between two short neighboring strands and between two adjacent layers. Comparing the influence of the two different process conditions, as expected, the samples processed with "High" setting 245/100/10/0.1 exhibit overall obviously higher temperature history and evidently longer time around the platform temperature than the corresponding values

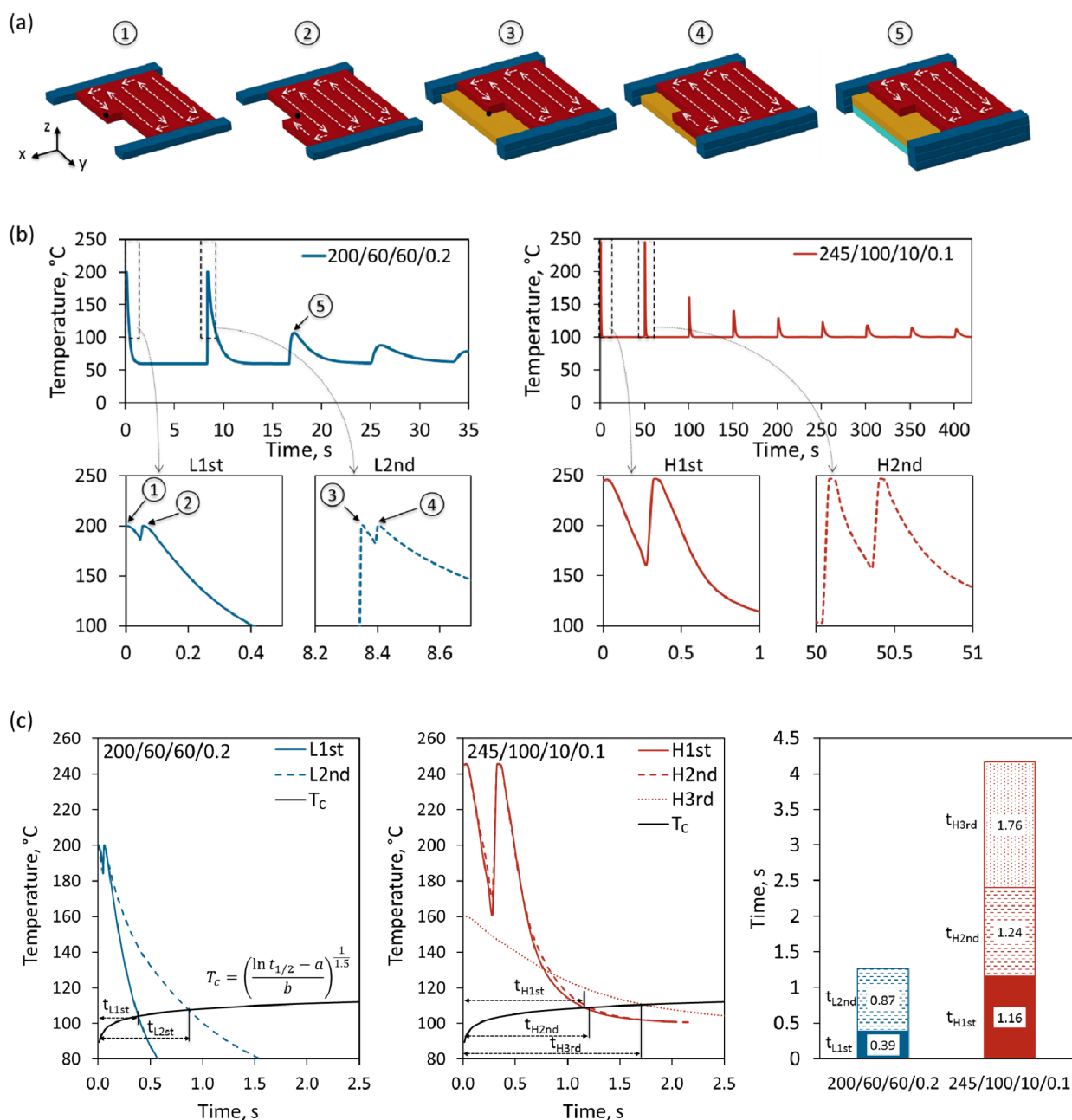


FIGURE 11 (a) Illustration of printing sequence in the center of the specimens printed with 200/60/60/0.2 (nozzle temperature/platform temperature/printing speed/layer height). The fixed black point (right) at $(x = 0 \text{ mm}, y = 0 \text{ mm}, z = 0.2 \text{ mm})$ was chosen for display the temperature profiles during the printing processes. (b) Temperature of the fixed point as a function of time for two different printing conditions: 200/60/60/0.2 (left), 245/100/10/0.1 (right). (c) Temperature at the fixed point and the T_c as a function of half-time of crystallization: 200/60/60/0.2 (left), 245/100/10/0.1 (middle). Comparison of the time above T_c (right) [Color figure can be viewed at wileyonlinelibrary.com]

of the samples with “Low” setting. It is generally accepted that crystallization process impedes the mobility of the polymer chains, and thus the time of the temperature at the weld area above the crystallization temperature (T_c) is a critical factor for the degree of interdiffusion of semicrystalline thermoplastics in the weld area.¹⁹ The half-time of crystallization ($t_{1/2}$),

defined as the time spent from the start of the crystallization process to the completion of half of the final total crystallization, which is usually used to determine the overall rate of the crystallization process directly. The dependency of the half-time of crystallization on the crystallization temperature of PP is given in a simplified equation⁴⁹:

$$t_{1/2} = e^{(a+bT_c^{1.5})} \quad (4)$$

where T_c is the crystallization temperature, $a = -17.094452$ and $b = 0.015177269$ are specific constants. The inverse function,

$$T_c = \left(\frac{\ln t_{1/2} - a}{b} \right)^{\frac{1}{1.5}} \quad (5)$$

that is, the crystallization temperature T_c as a function of half-time of crystallization and the temperature profiles at the reference point were plotted in Figure 11(c). The intercepts of this function with the cooling curves give an indication of how much time is available for crystallization under the given process conditions. As is seen, at the “Low” condition, the temperature curves L1st and L2nd show rapid cooling, reaching the T_c within 0.39 s (t_{L1st}) and 0.87 s (t_{L2nd}), respectively. In contrast, for the “High” condition, the H1st and H2nd temperature curves dropped to the T_c within 1.16 s (t_{H1st}) and 1.24 s (t_{H2nd}), respectively. Interestingly, under these conditions, passing over the reference point with the nozzle in the third layer again leads to remelting. Until cooling to T_c , 1.76 s (t_{H3rd}) are then available again.

Even though the absolute values may not perfectly match the real temperatures, it can be summarized that the total time of the temperature above the crystallization temperature at the “High” setting is about three times higher than the corresponding value at the “Low” setting. Even if only the last temperature peak is decisive for morphology formation, the “High” setting provides about twice as much time for crystallization. This inevitably leads to greater interdiffusion, uniform formation of spherulites (Figure 8(c)) and ultimately a homogeneous morphology (Figure 5(c), (d)), as is known from the solidification of quiescent melts of semi-crystalline polymers. Overall, this ultimately explains the better mechanical properties (Figure 3) under the “High” conditions.

4 | CONCLUSIONS

Both the morphology and the mechanical properties of void free 3D-printed polypropylene components are strongly dependent on the printing parameters. A larger heat input leads to a more homogeneous morphology and better mechanical properties. The welds clearly visible at low heat input have more stable nuclei, indicating high deformations and non-isotropic mechanical behavior as a result of processing. The simplified modeling and numerical simulation of the time-dependent three-

dimensional temperature distribution confirm the influence of heat (temperature) and allow a virtual parameter study. Overall, the welded joint between the strands determines the product quality. Good mechanical properties can be achieved if sufficient heat is introduced into the volume via the strand and the platform and this heat is dissipated again at a moderate rate, so that crystallization can take place in a quiescent melt with a largely balanced temperature field.

ACKNOWLEDGMENT

The authors are grateful to Borealis GmbH, Burghausen, for the donation of the material. Open Access funding enabled and organized by Projekt DEAL.

ORCID

Alois K. Schlarb  <https://orcid.org/0000-0001-8693-9163>

REFERENCES

- [1] J. M. Reverte, M. Caminero, J. M. Chacón, E. García-Plaza, P. J. Núñez, J. P. Becar, *Materials* **2020**, *13*, 1924.
- [2] R. Hashemi Sanatgar, C. Campagne, V. Nierstrasz, *Appl. Surf. Sci.* **2017**, *403*, 551.
- [3] S. Rohde, J. Cantrell, A. Jerez, C. Kroese, D. Damiani, R. Gurnani, L. DiSandro, J. Anton, A. Young, D. Steinbach, P. Ifju, *Exp. Mech.* **2018**, *58*, 871.
- [4] K. Raney, E. Lani, D. K. Kalla, *Mater. Today Proc.* **2017**, *4*, 7956.
- [5] M. J. Reich, A. L. Woern, N. G. Tanikella, J. M. Pearce, *Materials* **2019**, *12*, 1642.
- [6] M. Huang, J. Nomai, A. K. Schlarb, *eXPRESS Polym. Lett.* **2021**, *15*, 194.
- [7] K. Durgashyam, M. Indra Reddy, A. Balakrishna, K. Satyanarayana, *Mater. Today Proc.* **2019**, *18*, 2052.
- [8] G. Liao, Z. Li, Y. Cheng, D. Xu, D. Zhu, S. Jiang, J. Guo, X. Chen, G. Xu, Y. Zhu, *Mater. Des.* **2018**, *139*, 283.
- [9] L. Lin, N. Ecke, M. Huang, X. Pei, A. K. Schlarb, *Compos. Part B Eng.* **2019**, *177*, 107428.
- [10] A. Haleem, M. Javaid, *Clin. Epidemiol. Global Health* **2019**, *7*, 571.
- [11] O. S. Carneiro, A. F. Silva, R. Gomes, *Mater. Des.* **2015**, *83*, 768.
- [12] A. F. Silva, O. S. Carneiro, R. Gomes, *AIP Conf. Proc.* **2017**, *1896*, 040014.
- [13] L. Wang, D. J. Gardner, *Polymer* **2017**, *113*, 74.
- [14] Y. G. Zhou, B. Su, L. S. Turng, *Rapid Prototyping J.* **2017**, *23*, 869.
- [15] C. McIlroy, P. D. Olmsted, *Polymer* **2017**, *123*, 376.
- [16] J. E. Seppala, K. D. Migler, *Addit. Manuf.* **2016**, *12*, 71.
- [17] A. Goyanes, M. Kobayashi, R. Martínez-Pacheco, S. Gaisford, A. W. Basit, *Int. J. Pharm.* **2016**, *514*, 290.
- [18] C. S. Davis, K. E. Hillgartner, S. H. Han, J. E. Seppala, *Addit. Manuf.* **2017**, *16*, 162.
- [19] S. Hertle, M. Drexler, D. Drummer, *Macromol. Mater. Eng.* **2016**, *301*, 1482.
- [20] E. A. Papon, A. Haque, *J. Reinf. Plast. Compos.* **2018**, *37*, 381.
- [21] Q. Sun, G. M. Rizvi, C. T. Bellehumeur, P. Gu, *Solid Free. Fabr. Proc.* **2003**, *403*, 313.

- [22] M. Spoerk, J. Gonzalez-Gutierrez, C. Lichal, H. Cajner, G. R. Berger, S. Schuschnigg, L. Cardon, C. Holzer, *Polymers* **2018**, *10*, 490.
- [23] H. Xia, J. Lu, S. Dabiri, G. Tryggvason, *Rapid Prototyping J.* **2018**, *24*, 463.
- [24] Y. Shmueli, J. Jiang, Y. Zhou, Y. Xue, C.-C. Chang, G. Yuan, S. K. Satija, S. Lee, C.-Y. Nam, T. Kim, G. Marom, D. Gersappe, M. H. Rafailovich, *ACS Appl. Polym. Mater.* **2019**, *1*, 1159.
- [25] A. C. Abbott, G. P. Tandon, R. L. Bradford, H. Koerner, J. W. Baur, *Addit. Manuf.* **2018**, *19*, 29.
- [26] L. Wang, J. E. Sanders, D. J. Gardner, Y. Han, *Prog. Addit. Manuf.* **2018**, *3*, 205.
- [27] S. K. Padhi, R. K. Sahu, S. S. Mahapatra, H. C. Das, A. K. Sood, B. Patro, A. K. Mondal, *Adv. Manuf.* **2017**, *5*, 231.
- [28] V. E. Kuznetsov, A. N. Solonin, O. D. Urzhumtsev, R. Schilling, A. G. Tavitov, *Polymers* **2018**, *10*, 313.
- [29] D. Ravoori, H. Prajapati, V. Talluru, A. Adnan, A. Jain, *Addit. Manuf.* **2019**, *28*, 719.
- [30] S. Garzon-Hernandez, D. Garcia-Gonzalez, A. Jérusalem, A. Arias, *Mater. Des.* **2020**, *188*, 108414.
- [31] Q. Sun, G. M. Rizvi, C. T. Bellehumeur, P. Gu, *Rapid Prototyping J.* **2008**, *14*, 72.
- [32] S. F. Costa, F. M. Duarte, J. A. Covas, *J. Mater. Process. Technol.* **2017**, *245*, 167.
- [33] D. Bhalodi, K. Zalavadiya, P. K. Gurralla, *J. Braz. Soc. Mech. Sci. Eng.* **2019**, *41*, 113.
- [34] X. Wang, L. Zhao, J. Y. H. Fuh, H. P. Lee, *Polymers* **2019**, *11*, 1154.
- [35] H. Rezayat, W. Zhou, A. Siriruk, D. Penumadu, S. Babu, *Mater. Sci. Technol.* **2015**, *31*, 895.
- [36] L. Balzano, S. Rastogi, G. Peters, **2006** NSTI Nanotechnol. Conf. Trade Show - NSTI Nanotech 2006 Tech. Proc., *2*, 820.
- [37] A. K. Schlarb, D. N. Suwitaningsih, M. Kopnarski, G. Niedner-Schatteburg, *J. Appl. Polym. Sci.* **2014**, *131*, 39655.
- [38] B. Suksut, A. K. Schlarb, *J. Plast. Technol.* **2014**, *10*, 68.
- [39] J. Varga, J. Karger-Kocsis, *J. Polym. Sci. Part B Polym. Phys.* **1996**, *34*, 657.
- [40] M. Zhou, S. Xu, Y. Li, C. He, T. Jin, K. Wang, H. Deng, Q. Zhang, F. Chen, Q. Fu, *Polymer* **2014**, *55*, 3045.
- [41] R. M. Michell, A. Mugica, M. Zubitur, A. Muller, *J. Adv. Polym. Sci.* **2017**, *276*, 215.
- [42] J. A. Martins, W. Zhang, A. M. Brito, *Polymer* **2010**, *51*, 4185.
- [43] J. Kawabata, G. Matsuba, K. Nishida, R. Inoue, T. Kanaya, *J. Appl. Polym. Sci.* **2011**, *122*, 1913.
- [44] Y. Yu, F. Zeng, J. Chen, J. Kang, F. Yang, Y. Cao, M. Xiang, *Polym. Compos.* **2019**, *40*, E440.
- [45] M. Spoerk, F. Arbeiter, I. Raguž, G. Weingrill, T. Fischinger, G. Traxler, S. Schuschnigg, L. Cardon, C. Holzer, *Macromol. Mater. Eng.* **2018**, *303*, 1800179.
- [46] J. Varga, *J. Mater. Sci.* **1992**, *27*, 2557.
- [47] J. Varga, *J. Macromol. Sci. Phys.* **2002**, *41*, 1121.
- [48] P. Tordjeman, C. Robert, G. Marin, P. Gerard, *Eur. Phys. J. E: Soft Matter Biol. Phys.* **2001**, *4*, 459.
- [49] B. Suksut, A. Schlarb. Morphology and Morphology Formation of Injection Molded PP-based Nanocomposites, **2016**.
- [50] Baur; Brinkmann; Osswald; Rudolph; Schmachtenberg In Saechtling Kunststoff Taschenbuch, 119; **2013**.

SUPPORTING INFORMATION

Additional supporting information may be found online in the Supporting Information section at the end of this article.

How to cite this article: M. Huang, Y. Xu, A. K. Schlarb, *J. Appl. Polym. Sci.* **2021**, *138*(47), e51409. <https://doi.org/10.1002/app.51409>